Renewable and Sustainable Energy Reviews 151 (2021) 111606

Contents lists available at ScienceDirect

Renewable and Sustainable Energy Reviews

journal homepage: www.elsevier.com/locate/rser

Perovskite semiconductor-engineered cascaded molecular energy levels in naturally-sensitized photoanodes

Hisham A. Maddah [a,b], Lila Aryadwita [b], Vikas Berry [b], Sanjay K. Behura [c,d,*]

[a] Department of Chemical Engineering, King Abdulaziz University, Rabigh, 21911, Saudi Arabia
[b] Department of Chemical Engineering, University of Illinois at Chicago, 929 W. Taylor St., Engineering Innovation Building, Chicago, IL, 60607, United States
[c] Department of Chemistry and Physics, University of Arkansas at Pine Bluff, 1200 N. University Drive, Pine Bluff, AR, 71601, United States
[d] Department of Mathematics and Computer Science, University of Arkansas at Pine Bluff, 1200 N. University Drive, Pine Bluff, AR, 71601, United States

ARTICLE INFO

Keywords:
β-Carotene
Halide perovskite
Cosensitization
DSSC
Photoanode
Fermi level

ABSTRACT

Naturally-sensitized photoanodes in dye-sensitized solar cells (DSSCs) are promising alternatives to enhance photoabsorption, electron excitation/injection, but voltage loss remains a challenge. Here, we focus on understanding the cascading of energy levels in perovskite semiconductor cosensitized naturally-sensitized photoanodes to leverage forward charge transport addressing the voltage loss arising from ITO/TiO_2 heterojunction's built-in potential. The β-carotene-sensitized TiO_2 photoanode modified with methylammonium lead iodide ($MAPbI_3$) co-sensitizer causes an upward shifting in TiO_2 Fermi level (E_F). This phenomenon is predominantly attributed to increased initially injected electrons due to low $MAPbI_3$ bandgap and high visible-light absorption. Enhanced charge separation and injection mechanisms at the TiO_2/$MAPbI_3$ interface increase the effective density-of-states (DOS $>2.46 \times 10^{21}$ cm^{-3}) in the TiO_2 conduction band (CB) and hence decrease its work function to 4.82 eV. The decrease in TiO_2 work function suppressed CB bending at ITO/TiO_2 heterojunction, which minimized the photoinduced electrostatic potential barrier up to 13.1%. The reduced Schottky barrier ($\varphi_{SBH}<0.52$ eV) only allows electrons tunneling, while inhibited back-electron transport reduced both current leakage and voltage loss yielding in high open-circuit voltage (V_{oc} increase by 120%) and power conversion efficiency (PCE increase by 240%). The $MAPbI_3$ incorporation also broadened photoanode absorbance by 2-fold, paving the way towards perovskite semiconductor cosensitization to avoid voltage loss from bio-integrated photoanodes for photovoltaic and other optoelectronic and photonic applications. Future works will focus on studying the series resistance, cathode electrode coating uniformity, recombination kinetics, solid electrolytes, as well as other aspects typically related to increasing the photocurrent levels of this β-carotene-sensitized solar cell.

1. Introduction

Photosensitization is the basis for designing efficient dye-sensitized solar cells (DSSCs) capable of initiating electron injection and charge transfer from the LUMO energy level of dye molecules to the conduction band (CB) of the wide band gap (WBG) semiconductor [1–3]. Different kinds of natural and environmental-friendly photosensitizers [4] extracted from light-harvesting (LH) complexes of anthocyanin, carotenoid, and chlorophyll biomolecules [5] have emerged as an attempt to substitute the expensive and toxic [6] ruthenium polypyridyl dyes [7]. However, the power conversion efficiency (PCE) of bio-sensitized DSSCs is low (<0.05–1.7%) [8–10] and requires a thorough understanding of the role of pigment's molecular structure, interfacial interactions, anchoring groups, and conjugated double bonds (n) in dye attachment, improved carriers transport, and decreased recombination [11–13]. Surface hydroxylation [14–16], perovskite cosensitization [17–20], and/or absorbance expansion were previously utilized to improve electron injection and photoanode sensitization, respectively. Enhanced photoanode sensitization and broadened photoanode absorption spectrum [21] is attainable by stacking semiconducting materials [22–24] with different bandgaps, or more viably by utilizing low-bandgap energy cosensitizers [17–20]. Methylammonium lead iodide ($MAPbI_3$) perovskite semiconductors [25,26] are appropriate for cosensitization functionalities owing to their high visible-light absorption ($\alpha = 0.7 \times 10^7$ cm^{-1}) [27], composition-engineered bandgap tunability (E_g = 1.5∼ 2.43 eV) [28], high charge carriers mobility (>5 cm^2 V^{-1} S^{-1}) [29], long diffusion lengths (>100 nm) [30], and easy processability

* Corresponding author. Department of Chemistry and Physics, University of Arkansas at Pine Bluff, 1200 N. University Drive, Pine Bluff, AR, 71601, United States.
E-mail address: behuras@uapb.edu (S.K. Behura).

https://doi.org/10.1016/j.rser.2021.111606
Received 12 December 2020; Received in revised form 18 July 2021; Accepted 23 August 2021
Available online 1 September 2021
1364-0321/

Nomenclature

Abbreviation/unit Jargon

DSSCs	Dye-sensitized solar cells
LH	Light-harvesting
PCE (η)/%	Power conversion efficiency
$MAPbI_3$	Methylammonium lead iodide
D−π−A	Donor−π−acceptor
CB	Conduction band
V_{oc}/V	Open circuit voltage
φ_{SBH}/eV	Schottky barrier height
WBG	Wide bandgap
MAI	Methylammonium iodide
CEs	Counter electrodes
ETL	Electron transport layer (TiO_2)
P	Perovskites ($MAPbI_3$)
HTL	Hole-transport layer
TE	Thermionic emission
J-V	Current density-voltage
n	Diode ideality factor
RFs	Rectification factors
J_0/nA	Dark saturation current (leakage)
FF	Fill factor
R_s/kΩ	Series resistance
R_{sh}/kΩ	Shunt resistance
J_{sc}/μA cm^{-2}	Short circuit current density
J_1/μA cm^{-2}	Apparent current density in both TiO_2 and $MAPbI_3$
J_2/μA cm^{-2}	Total apparent current density in the electrolyte solution [I^-/I_3^-]
α/cm^{-1}	Absorption coefficient
$h\nu$/eV	Photon energy
E_g/eV	Bandgap
t /mm	Thickness of the quartz cuvette
OD/cm^{-1}	Optical density
λ_{max}/cm^{-1}	Maximum absorption wavelength
V_1/V	Voltage loss
E_F/eV	Fermi level
[I^-/I_3^-]	Liquid redox electrolyte
φ_{TiO_2}/eV	TiO_2 work function
THF	Tetrahydrofuran

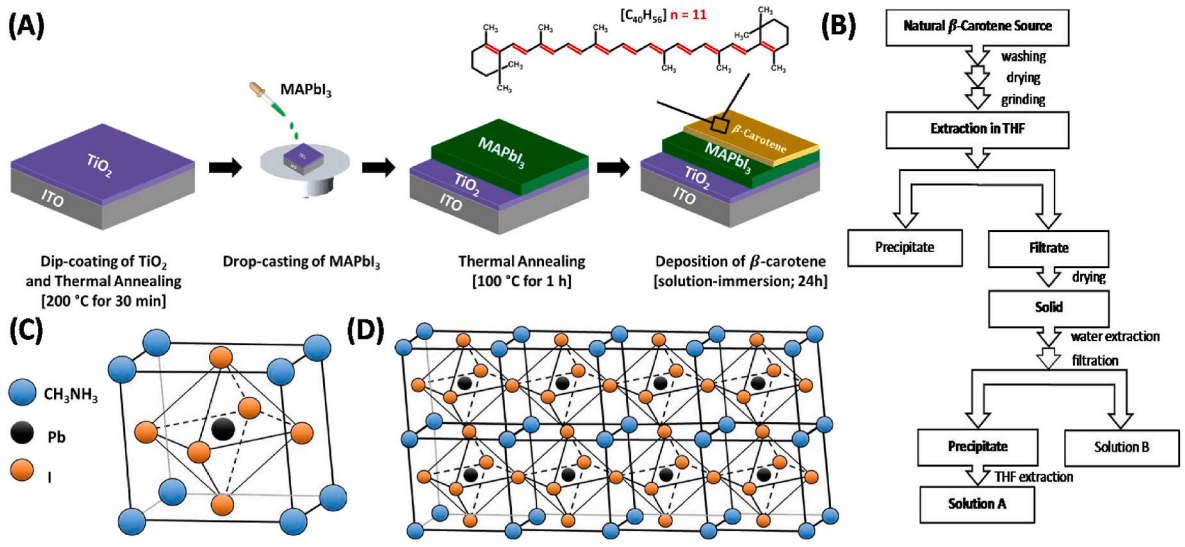

Fig. 1. **(A)** Experimental steps for the fabrication of [ITO/TiO_2/$MAPbI_3$/β-carotene] photoanode heterostructure; **(B)** Flowchart showing the THF-extraction procedure and step-wise purification for β-carotene; **(C)** Organic-inorganic halide perovskite ($MAPbI_3$) unit cell; **(D)** Ideal cubic structure for $MAPbI_3$ when (tolerance factor = 1) indicating a perfect cation fit.

[31,32]. Combining $CH_3NH_3PbX_3$ (X = Br or I) in a TiO_2-based photoanode has shown its potential to achieve high efficiency with Ru-dyes in a liquid-state (3.81%) [17], quantum-dot-sensitized (6.54%), and a solid-state mesoscopic DSSC (15%) [33]. However, such cosensitization has not been yet studied with natural biomolecular dyes, according to the authors' knowledge, for potential improvements in bio-sensitized DSSCs.

In this work, we focus on understanding the role of perovskite cosensitization and its interfacial interaction with TiO_2 and β-carotene in leveraging forward charge transport. Such cosensitization can address the voltage loss arising from ITO/TiO_2 heterojunction's built-in potential in bio-sensitized DSSCs. We elucidated the photoabsorption mechanisms [34] pertaining cosensitization of β-carotene pigments. The integration of organic-inorganic $MAPbI_3$ halide perovskites with β-carotene dyes have been studied using a novel naturally-sensitized photoanode in [ETL/Perovskite/HTL] configuration in liquid-state DSSCs. Perovskite cosensitizers improved PCE *via* enhancing visible-light absorption, excitons generation, electron injection, and reducing voltage loss at ITO/TiO_2 junction. Broadening of the absorbance spectrum is expected for the cosensitized photoactive layers increasing the probability of absorbing more photons within (400–700 nm) [35] from the available 42% visible-light energy in solar radiation [36]. Experimental procedures for the design of [ITO/TiO_2/-$MAPbI_3$/β-carotene] photoanode are shown in Fig. 1-A. The THF-solvent dye extraction and step-wise purification of non-treated lab-grade β-carotene powders (Sigma Aldrich, USA) are illustrated in Fig. 1-B, to obtain "Solution A″ which was used for β-carotene deposition atop $MAPbI_3$. The $MAPbI_3$ unit cell and crystal structure consist of a cubic array with A-site corners sharing BX_6 octahedra are shown in Fig. 1-C and Fig. 1-D.

2. Carotenoids and perovskites cosensitization

Poly-isoprenoid carotenoids (e.g. xanthophylls, lycopene, and β-carotene) hold great potential as natural photosensitizers in DSSCs [11,21]. Carotenoids contain double π-conjugated bonds (n > 11) responsible for visible-light photoexcitation (400–550 nm and 620–680 nm) [37] of free electrons to higher energy levels (π to π^*) [38]. However, donor−π−acceptor (D−π−A) conjugated carotenoid dye molecules [9,39] have poor surface interactions and/or chemisorption onto TiO_2. The poor dye attachment hinders effective electron injection into the TiO_2 CB resulting in low PCE for carotenoids <0.58% [8] (<0.074% for β-carotene [9]). Onodera et al. showed that the open-circuit voltage (V_{oc}) decreased with increasing Schottky barrier height (φ_{SBH}) at the interface of TiO_2 and transparent conducting oxide (TCO) [40–42]. In DSSCs, TCO is the base substrate on which the cell is built and it allows the light to enter into the solar cell. TCOs used in DSSCs are indium tin oxide (ITO), fluorine-doped tin oxide (FTO), aluminum-doped zinc oxide (AZO), and gallium-doped zinc oxide (GZO). In this study, when TiO_2 comes in contact with ITO, band bending in TiO_2 CB occurs influencing the current-loss mechanism from inhibited electron collection. Perovskite cosensitization can promote the β-carotene sensitized-photoanode light-harvesting ability addressing both TiO_2 CB bending and voltage loss problems. This is because perovskite cosensitization mitigates interfacial recombination and CB bending in TiO_2 (reduced φ_{SBH}) due to the $CH_3NH_3PbI_3/TiO_2$ interactions. However, weak dye attachment lowers the performance of bio-DSSCs from electron recombination at the dye/semiconductor interface [8,21,43]. One may be able to study changes in the $MAPbI_3$ film and/or β-carotene anchoring either by hydrogen bonding or chemisorption from the FT-IR analysis of the available bonds. Interfacial recombination with the oxidized dye or oxidized redox species in the electrolyte [44] facilitates current leakage that is the main limitation for improving PCE of naturally-sensitized DSSCs [11]. Missing and/or few dye anchoring groups (− OH or − COOH) in the acceptor segments [12] lead to high series resistance and reduced current density (J_{sc}∼ μA/cm^2) [45]. These observations contribute in increasing the voltage loss from φ_{SBH} at the ITO/TiO_2 interface (n-type semiconductor/metal) resulting in internal resistance and recombination current with the electrolyte. Thus, strong van der Waals interactions possibly introduced by $MAPbI_3$ ensure fast electron injection completed within 100 fs (with possible improved dye attachment on $MAPbI_3$), where $CH_3NH_3PbI_3/TiO_2$ covalent bonding should facilitate photoexcitation of charge-separated states leading to ultrafast interfacial charge separation prior to electron injection [46].

Recent studies (2018–2020) showed the potential of using carotenoids including β-carotene as biomolecular sensitizers in photoanode structures. For instance, Zanjanchi and Beheshtian (2019) showed in their recently published theoretical work, based on density functional theory (DFT), that carotenoids are considered as an optimal natural pigment class to achieve high open-circuit photovoltage [47]. Further, experiments have backed-up this theory showing the possibility to have a PCE as high as 2% from using a cocktail of naturally-sensitized dyes (e.g. chlorophyll, betanins, carotenoids, anthocyanins, and tannins), which enhanced photoanode visible-light absorption abilities [48]. Moreover, the use of cobalt solid-state redox with novel metal-free dihexyloxy-substituted triphenylamine (DHO-TPA) dye has shown a significant improvement in dye attachment and cell stability allowing achievement of a cell performance of up to 10.3% [49]. However, when focusing on studying β-carotene alone as a natural β-carotene photosensitizer in DSSCs, recent works from the last three years showed a maximum PCE of 0.074% in [FTO/TiO_2/β-carotene/[I^-/I_3^-]/Pt/FTO] with a current density of 270 μA cm^{-2} and V_{oc} = 400 mV [9]. This relatively high PCE from β-carotene only (i.e. considered high when compared to DSSCs made of natural pigments) was achieved from using EL-HSE (triiodide/iodide imidazole compound in 3-methoxypropionitrile for high stability redox, Dyesol) interfaced with β-carotene dye molecules with a bandgap around 2.47 eV, where the dye was extracted from Syngonium leafs [9]. Another study (2018) showed that β-carotene extracted from yellow sweet potato was capable of absorbing visible-light energy in the range 400–550 nm within a designed [FTO/-TiO_2/β-carotene/[I^-/I_3^-]/Pt/FTO] DSSC heterostructure achieving a maximum PCE of 0.057% [6]. A much recent study (2019) used readily available lab-grade β-carotene powders in a regular [ITO/-TiO_2/β-carotene/[I^-/I_3^-]/C/ITO] liquid-redox-based DSSCs which showed PCE of 1 × 10^{-4}% [50], meanwhile, Supriyanto et al. (2018) found that extracted β-carotene dyes from orange fruit and tomatoes applied in [FTO/TiO_2/β-carotene/[I^-/I_3^-]/Pt/FTO] would show PCEs of 0.02% and 0.03%, respectively, with maximum absorption wavelength around 441 and 466.5 nm [21]. Furthermore, the blending of chlorophyll with carotenoids has shown a much improvement in carotenoids sensitizing function in DSSCs since chlorophyll provides intensified visible-light absorption capabilities with enhanced layer protection [51,52] and formed radical cations [53]. Protein complexes (LH2, BR, RC) and chlorophyll-a combined with carotenoids showed a high DSSCs PCE of 0.16–0.57% and 4%, respectively.

3. Materials and methods

3.1. TiO_2 deposition (dip-coated or spin-coated) on ITO photoanodes

ITO substrates (1″ transparent and conductive sheets with sheet resistance of ∼ 23 Ω/■) were sonicated in IPA for 15 min and followed by deionized (DI) water washing. Scotch tapes were applied on the conductive sides to have a 2 cm × 1.5 cm exposed surface area ready for TiO_2 dip-coating (or spin-coating) with no prior treatments for TiO_2 nanoparticles paste (Sigma Aldrich, USA). With taped ITO backsides, ITO sheets were dip-coated (or spin-coated @ 3000 rpm) successively, removed immediately, and dried in ambient air for 5 min before annealing the ITO/TiO_2 structure at 400 °C for 30 min [54]. TiO_2 crystals forming above >270 °C may induce a significant increment of R_s of ITO layer yielding in extremely low photocurrents. Crystallized TiO_2 nanoparticles atop ITO films were removed from the hot plate, rinsed with DI water, and stored in a dry petri dish.

3.2. Synthesis of $MAPbI_3$ and deposition

$MAPbI_3$ was synthesized by mixing 2 g of PbI_2 powders with 0.5 g of MAI powders in a glass beaker with continuous addition of 5 mL of DMF under standard conditions [31,32]. The mixed solution was then heated on a hot plate for 1 h at 60 °C under vigorous stirring. The obtained precursor was drop-casted (2–3 drops) onto sintered ITO/TiO_2 electrodes and crystallized at 100 °C for 1 h to obtain the ITO/TiO_2/$MAPbI_3$ heterostructure.

3.3. THF-extraction of β-carotene sensitizers and deposition

Since the solubility of β-carotene carotenoids is greatest in tetrahydrofuran (THF), 10,000 mg/L [55], among other organic solvents, THF solvent was utilized for dye extraction and step-wise purification of non-treated lab-grade β-carotene powders (Sigma Aldrich, USA) [56]. β-carotene powders (1.5 mg) were added to THF organic solvent (50 mL) under continuous stirring for 1 h in ambient conditions. Dye extraction was confirmed from the observed color change in the THF (yellowish/reddish). THF solvent was then vacuum filtered, dried, and washed with DI water following the step-purification using the procedure shown in Fig. 1(B) to obtain THF–H_2O–extracted carotenoid precipitates. Purified carotenoids were then washed again with THF (50 mL) to obtain "Solution A″ used for dye deposition. Solution A was concentrated at 60 °C (THF volume reduced to 25 mL). All sintered photoanodes were soaked in THF-β-carotene concentrated solution for >24 h to ensure dye deposition and molecules anchoring onto TiO_2 *via* covalent bonding

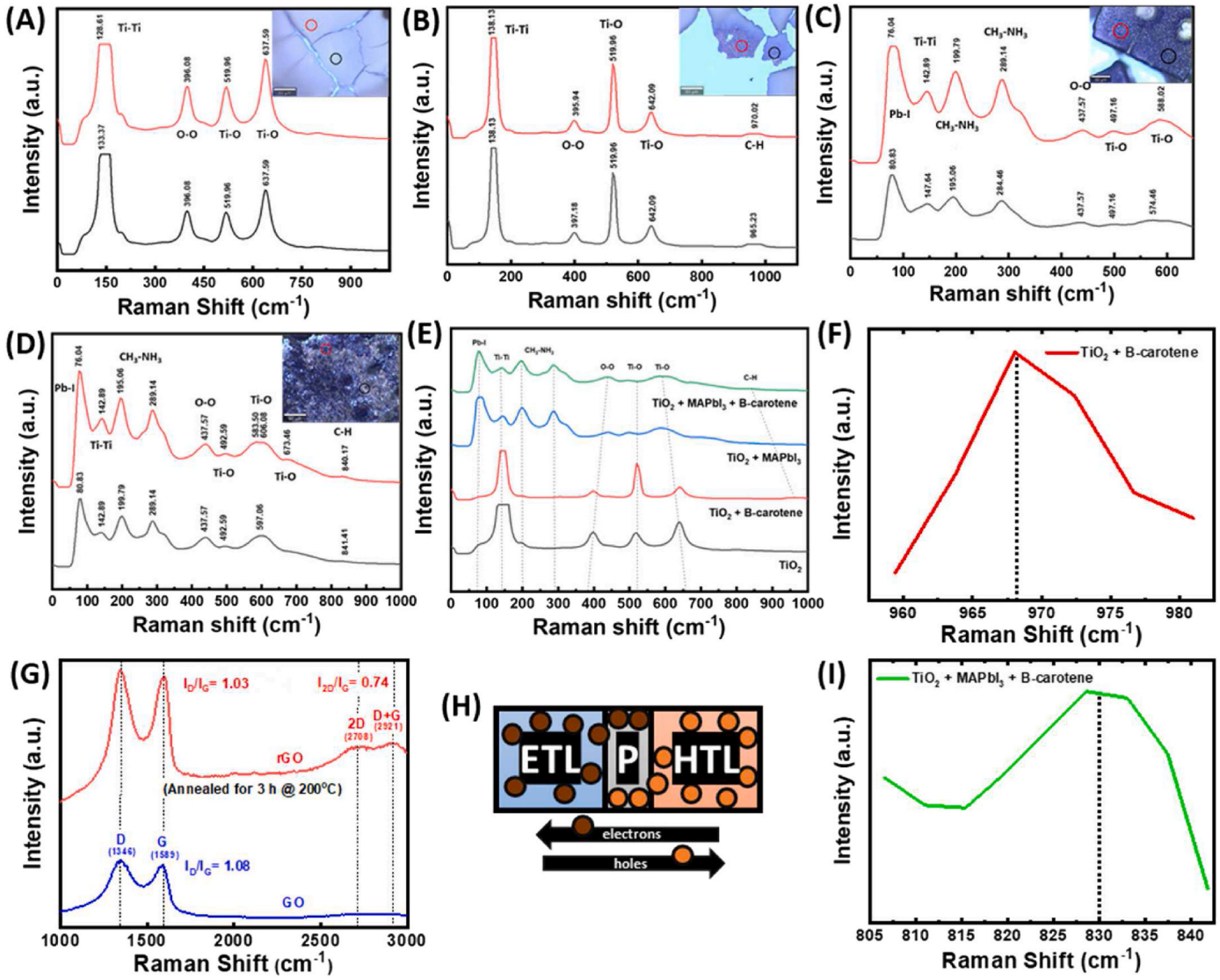

Fig. 2. Single-spectrum Raman spectroscopy characterization of different nanostructured naturally-sensitized photoanodes: **(A)** ITO/TiO_2; **(B)** ITO/TiO_2/β-carotene; **(C)** ITO/TiO_2/$MAPbI_3$; and **(D)** ITO/TiO_2/$MAPbI_3$/β-carotene, **insets in A-D:** optical images and Raman scan locations; **(E)** Comparison of Raman bands observed in the four photoanode surfaces showing energy-shifts (red- or blue-shifted) in TiO_2 and β-carotene when combined with $MAPbI_3$ co-sensitizer; **(F)** and **(I)** Zoom-in on the (v_3) vibrational bands of β-carotene from C–H rocking before and after $MAPbI_3$ interfacing; **(G)** Single-spectrum Raman spectroscopy characterization for the synthesized coal-derived GO and the annealed ITO/GO yielding in rGO-cathode electrodes; **(H)** Schematic showing the possible excitons generation and electron/hole transport layers involved in perovskite-cosensitized DSSCs; ETL: electron transport layer (TiO_2); P: Perovskites ($MAPbI_3$); HTL: hole-transport layer (β-carotene/$[I^-/I_3^-]$).

and/or possible chemisorption.

3.4. Synthesis of coal-derived rGO for cathode

$NaNO_2$ was used as a weak oxidant to avoid structural damages while breaking the van der Waals interlayer forces that exist between the coal-based graphitic layers. 2.5 g of coal sample was oxidized with 2 g of $NaNO_2$ in 100 mL of H_2SO_4 (98%). The suspension was agitated for 24 h at room temperature conditions; followed by heating up to 80 °C and stirring for 6 h. HNO_3 (1 M) was added to the suspension and then diluted with DI water (volume ratio of 1:2) to promote chemical exfoliation. The resultant graphene oxide (GO) suspension was centrifuged (1000 rpm) for 15 min to discard the undesired ions. The supernatant was dispersed in DI water and centrifuged (12,000 rpm) to collect precipitates (3-times) and to remove the remaining impurities. The counter electrode (cathode) was created by drop-casting (2–3 drops) of the coal-derived GO suspension on the conductive side of ITO. Drop-casted GO (post-deposited on ITO) was then chemically reduced in a vacuum oven by annealing at 200 °C for 3 h to remove the undesired oxygen (=O), hydroxyl (–OH), and carboxyl (–COOH) functional groups yielding in reduced graphene oxide (rGO) blackish films.

3.5. Cell fabrication and photovoltaic measurement

Four DSSC cell designs are considered for the performance analysis: (a) ITO/TiO_2/$[I^-/I_3^-]$/rGO/ITO; (b) ITO/TiO_2/β-carotene/$[I^-/I_3^-]$/rGO/ITO; (c) ITO/TiO_2/$MAPbI_3$/$[I^-/I_3^-]$/rGO/ITO; and (d) ITO/TiO_2/$MAPbI_3$/β-carotene/$[I^-/I_3^-]$/rGO/ITO; as illustrated in Figure S4. A drop of $[I^-/I_3^-]$ liquid redox electrolyte was drop-casted on the TiO_2-photoanode. Both photoanode and cathode were brought together while keeping the conductive ITO sides facing each other with a careful line-up of TiO_2-anode on rGO-cathode. Once the line-up was satisfied, binder clips were applied on the cell sides to hold the DSSCs in place. An offset was kept between the two electrodes to connect Cu-tapes electrical

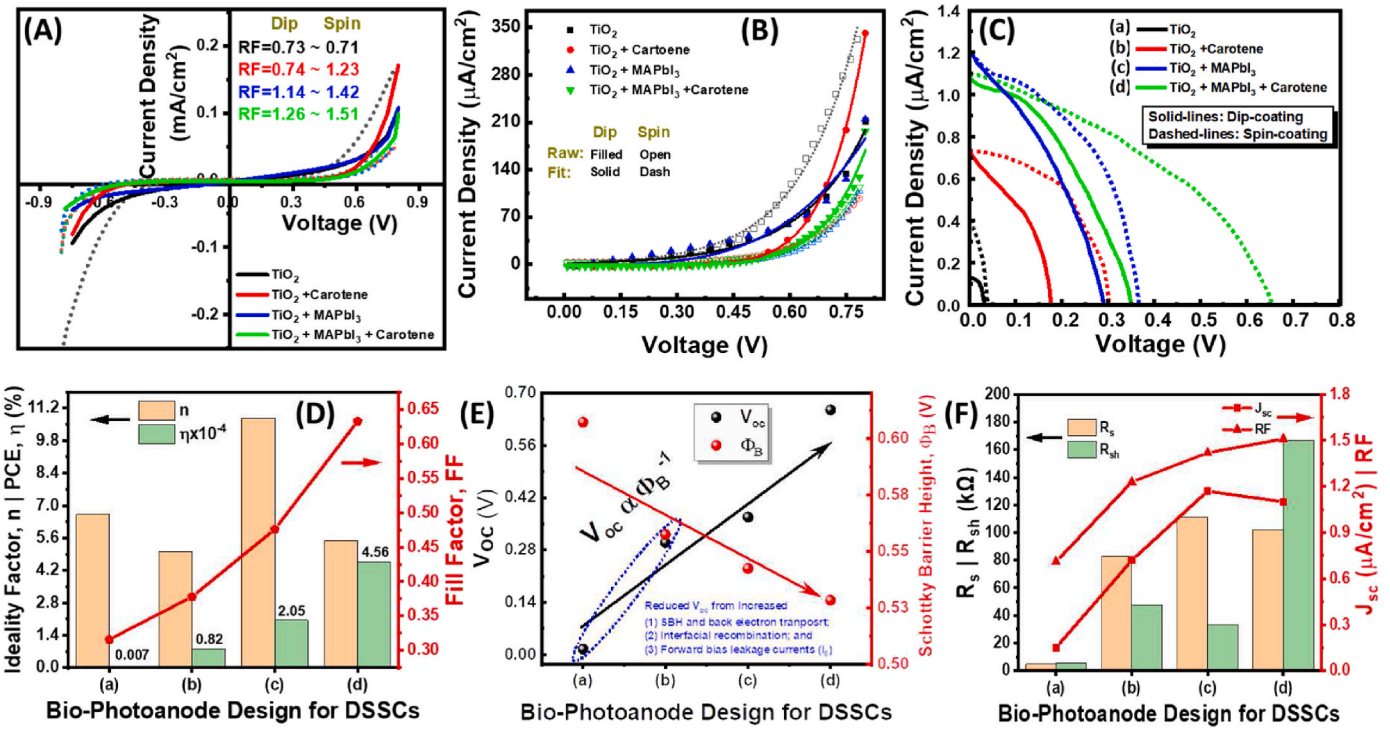

Fig. 3. Different nanostructured photoanodes for β-carotene-sensitized and/or $MAPbI_3$ cosensitized bio-DSSCs: **(A)** Diode behavior and rectification factors (RFs) with highest RF≈1.5 reserved for spin-coated photoanode with sensitized/cosensitized DSSC reducing dark saturation currents (J_0); **(B)** Exponential fitting of forward-current using the TE diode model for analyzing diode ideality (n) factors; **(C)** J-V curves and photovoltaic effect with highest V_{oc}≈0.66 V reserved for DSSC with spin-coated sensitized/cosensitized photoanode; **(D)** Calculated ideality factor (n), power conversion efficiency (PCE), and fill factor (FF) for DSSCs with different spin-coated photoanodes (a)–(d); **(E)** Relationship between V_{oc} and ITO/TiO_2 φ_{SBH} in spin-coated samples showing reduced φ_{SBH} from addition of $MAPbI_3$ co-sensitizers resulting in high built-in potential and upward shifting of TiO_2 Fermi level; **(F)** R_s, R_{sh}, J_{sc}, and RF observed in DSSCs with different spin-coated photoanodes (a)–(d).

contacts at the positive and negative terminals creating a complete electric circuit ready for current-voltage (J-V) analysis [54]. Diode and photovoltaic measurements were carried out in the room temperature conditions with a source meter (Keithley 2612); current density versus voltage (J-V) measurements of designed solar cells were performed under 100 mW/cm^2 illuminations (AM1.5G) using a solar simulator.

3.6. Raman spectroscopy

Raman spectroscopy characterization of photoactive electrode materials was performed using a confocal Raman microscope (Raman-AFM, WITec alpha 300 RA, laser wavelength of 532 nm). Single-spectrum analyses were carried out using a laser spot-size of about 700 nm and 20X objective lens.

3.7. Absorption spectrum of $MAPbI_3$, TiO_2, and β-carotene

Absorption spectrums of photoactive materials were measured using a UV–Vis spectrophotometer (SSEYL UV-5100, ±2 nm). DI water was used as a reference solution for the baseline of the absorption spectrum of $MAPbI_3$ and TiO_2, whereas THF-solvent was used as a reference solution for β-carotene absorption measurements. First, DI-water (10 mL) reference solution spectrum was measured for baseline correction. Then, a drop of $MAPbI_3$ or TiO_2 was added to each of the two separate cuvettes filled with DI (10 mL), located in front of the UV–Vis light to measure the optical absorption spectrum. Similarly, a drop of β-carotene was added to THF-solvent (10 mL) reference solution for the β-carotene absorption spectrum analysis. Three runs of each solution were measured for accuracy. Lastly, calculations of the cumulative fit peak for all the above three solutions' absorption spectrum were performed to estimate the photoanode optimal wavelength absorption abilities.

4. Results and discussion

Raman spectroscopy characterization (532 nm laser excitation) of bulk TiO_2 in the anatase phase reveals evident vibrational modes at 638, 520, 396, and a very distinct peak at 129 cm^{-1} (Fig. 2) confirming the deposition of TiO_2 layer on ITO substrate. The space group D_{4h}^{19} is attributed to anatase phase with assumed site symmetries for the Ti and O atoms within the unit cell (D_{2d} for Ti; C_{2v} for O). The group-theory analysis shows six Raman-active "lattice vibrations" assigned as follows: A_{1g} (517 cm^{-1}), B_{1g} (640 cm^{-1}), B_{1g} (397 cm^{-1}), E_g (640 cm^{-1}), E_g (147 cm^{-1}), and E_g (197 cm^{-1}) [57]. The distinct peaks at 128∼ 134 cm^{-1} indicate the vibrations of Ti–Ti bonding in the octahedral chains. The band at 396 cm^{-1} represents the O–O covalent interactions in TiO_2, where covalence/length/frequency relation calculations confirm the Ti–O band occurrence at 638 and 520 cm^{-1} [58]. Broader and shifted peaks were observed in Fig. 2-E for Ti–O (638 cm^{-1}) and O–O (396 cm^{-1}) vibrations from the addition of $MAPbI_3$ and/or β-carotene photosensitizers. The O–O band is blue-shifted while the Ti–O band is red-shifted indicating changes in the energy requirements for Raman-active polarizable vibrations. In Fig. 2-(C-E), we observed the Raman spectra of $MAPbI_3$ with two prominent peaks: (i) the vibrational mode at 76∼ 80 cm^{-1} (theoretically ∼ 110 cm^{-1}) is attributed to the Pb–I stretching and bending of the Pb–I–Pb bond with either A_g or B_{2g} symmetry, and (ii) the bands at 200 and 300 cm^{-1} (theoretically ∼ 250 cm^{-1}) indicate the liberations of the MA cations (MA torsional modes) [59,60]. No red-shifts were observed in perovskite peaks when $MAPbI_3$ was interfaced with other photoanode materials confirming stress-free/undeformed perovskite crystals and preserved $MAPbI_3$ photosensitivity. Thampy et al. [61] proved that the use of [$MAPbI_3$ + TiO_2] ∼ $MAPbI_3$ provides the highest interfacial stability, indicated by decomposition temperature, as compared to [$MAPbI_3$ + SnO_2] >

Table 1
Determined diode parameters and φ_{SBH} at the ITO/TiO_2 interface in the different designed DSSCs using various naturally-sensitized and/or cosensitized photoanode architectures.[a]

(SN) Photoanode Architecture	Coating	J_0 (μA)	n	RF	φ_{SBH} (V)	J_1 (pA)	J_2 (μA)
(a) TiO_2	Dip	2.280	5.97	0.73	0.607	0.274	0.150
	Spin	1.870	6.62	0.71	0.607	0.143	0.150
(b) TiO_2 + **β**-carotene	Dip	0.364	5.40	0.74	0.559	N/A	N/A
	Spin	**0.002**	**5.00**	1.23	0.557	N/A	N/A
(c) TiO_2 + $MAPbI_3$	**Dip**	**0.006**	**4.03**	1.14	**0.542**	**423.2**	**1.330**
	Spin	0.041	10.76	1.42	0.542	3.988	1.170
(d) TiO_2 + $MAPbI_3$ + **β**-carotene	**Dip**	0.173	4.67	**1.26**	0.544	N/A	N/A
	Spin	0.081	5.47	**1.51**	**0.528**	N/A	N/A

The bolded numbers refer to the optimal found design parameters for achieving high solar cell efficiency based on the selected photoanode and coating method.
[a] $R^2 > 0.99$ in the different cells using TE diode equation against curves exponential fitting [$y = a\exp(bx)$]; φ_{SBH} at ITO/TiO_2 from Eq. (S7) in Supplementary (see section 4) from the measured J_{sc} and $V_{oc} = V_1$ reported in Table 2; J_1 is the apparent current density in both TiO_2 and $MAPbI_3$, J_2 is the total apparent current density in the electrolyte solution [I^-/I_3^-] from electron diffusion, calculated @ corresponding reported diffusion coefficients (D_e) and charge/electron densities or number of electrons (n_e) of materials from literature (Supplementary, see section 4).

[$MAPbI_3$ + NiO] contacts. Methylammonium iodide (MAI) DFT calculations and experiments showed the strongly bound $MAPbI_3$ molecules on the TiO_2 surface preventing further reactions [61]. This comes in agreement with the observed stress-free/undeformed $MAPbI_3$ crystals deposited on TiO_2 suggesting equivalent $MAPbI_3$ bulk decomposition rates for [$MAPbI_3$ + TiO_2] ~ $MAPbI_3$ for reduced interfacial recombination and improved device stability. It turned out that the interactions between perovskite and TiO_2 at 0 K are purely van der Waals, whereas I–Ti covalent bonds can form transiently at the interface at ambient temperatures according to time-domain DFT calculations. The strong interactions between the donor and acceptor species at $CH_3NH_3PbI_3$/-TiO_2 interface ensure fast electron injection completed within 100 fs [46]. The covalent bonding contributes to the high efficiencies of perovskite-sensitized TiO_2 solar cells due to facilitated photoexcitation of charge-separated states and adiabatic electron transfer leading to ultrafast interfacial charge separation [46].

The Raman spectra of β-carotene show a weak band at 970 cm^{-1} (v_3) due to the in-plane rocking modes of the CH_3 groups attached to the polyene chain and C–H bending, Fig. 2-(B-E) [62,63]. Interestingly, when β-carotene was combined with either TiO_2 and $MAPbI_3$, we observed that there is a strong red-shift of about 130 cm^{-1} in the weak band of β-carotene as shown in Fig. 2-(F,I). This red-shifting might indicate stresses in the β-carotene structure induced by hydrogen-bonding and/or dipole-dipole van der Waals interactions of C–H bond with $MAPbI_3$ crystal lattice.

To build a cost-effective bio-DSSC, we have further employed coal as a natural carbon source to create rGO-based counter electrodes (CEs). Coal-derived GO and rGO CEs were characterized from the D-peak at 1346 cm^{-1}, which corresponds to the A_{1g} breathing vibration mode, activated by the structural defects and disordered sp^2 domains in graphene lattice, the G-peak at 1589 cm^{-1}, which corresponds to the in-plane E_{2g} vibration mode of neighboring carbon atoms of sp^2-hybridized C=C bonds, and the 2D peak at 2708 cm^{-1}, which corresponds to the overtone of the D-band resulting from the double-resonance two-phonon in-elastic scattering process [64,65]. The intensity ratio of 2D and G-bands ($I_{2D}/I_G \approx 0.74$) confirming the existence of a multi-layered graphene structure (Fig. 2-G). The charge transport layers involved in perovskite-cosensitized bio-DSSCs, modified with [ETL/Perovskite/HTL] configuration, are shown in Fig. 2-H.

To quantify the diode and photovoltaic parameters, thermionic emission (TE) [66,67] and Cheung's methods [68] are typically used. The cell diode parameters were determined from the exponential fitting of dark current density-voltage (J-V) data (dark current) following the TE model: $J_D = J_0 \exp\left(\frac{qV}{nk_BT}\right)$, (Fig. 3-B), where symbols definitions can be found in Supplementary (see sections 1 and 2). The diode ideality factor (n) approached unity by $MAPbI_3$ and/or β-carotene photoanode sensitization reaching optimal n = 4–5, due to reduced current leakage (J_0). Dark saturation currents (J_0) are found to approach the nano-amperes (nA) range when adding $MAPbI_3$ and/or β-carotene yielding less leakage current as shown in Table 1 or Fig. 3-A and Fig. 3-D for spin-coated photoanode cells. A lower n value indicates better electron transport from reduced recombination at the interfacial contacts. Reproducibility of the diode curves was obtained for the same photoanode (see Supplementary, Figure S1). Sensitized/cosensitized DSSCs diodes showed the highest RF≈1.2–1.5 indicating a two-fold increase in [forward/reverse] photocurrents compared to only-TiO_2 photoanodes (Fig. 3-A). The φ_{SBH} of ITO/TiO_2 junction was also diminished matching the expected high V_{oc} (Fig. 3-E). However, the very low photocurrents ~ μA/cm^2 in fabricated devices might be correlated to the perovskite crystals decomposition (suggesting higher $MAPbI_3$ bandgap). Such decomposition of deposited layers is possible due to the introduced interfaces in the photoanode structure: (i) TiO_2/$MAPbI_3$, (ii) TiO_2/-$MAPbI_3$/dye, (iii) TiO_2/$MAPbI_3$/electrolyte, and (iv) TiO_2/$MAPbI_3$/dye/electrolyte. The complicated structure would alter the existing material's structural bonds yielding possible films degradations and/or corroded $MAPbI_3$ from being in contact with the electrolyte. In an optimal photoanode heterostructure, the $MAPbI_3$ should be completely sandwiched by the deposited TiO_2 nanoparticles and β-carotene to avoid undesired interactions between the $MAPbI_3$ layer

Table 2
DSSCs photovoltaic parameters in DSSCs using different photoanode heterostructures.

(SN) Photoanode Architecture	Coating	R_s (kΩ)	R_{sh} (kΩ)	V_{oc} (V)	J_{sc} (μA/cm^2)	FF	**η** (%)
(a) TiO_2	Dip	<33.3	55.56	0.015	0.15	0.24	5.47×10^{-7}
	Spin	<4.76	5.56	0.015	0.15	0.32	7.11×10^{-7}
(b) TiO_2 + **β**-carotene	Dip	83–129	37.04	0.171	0.80	0.30	4.16×10^{-5}
	Spin	83–129	47.62	0.300	0.72	0.38	8.22×10^{-5}
(c) TiO_2 + $MAPbI_3$	Dip	**55–84**	33.33	0.290	**1.33**	0.33	1.29×10^{-4}
	Spin	111–168	33.33	0.368	**1.17**	0.48	2.05×10^{-4}
(d) TiO_2 + $MAPbI_3$ + **β**-carotene	Dip	**51–83**	41.67	**0.341**	1.14	**0.36**	**1.40×10^{-4}**
	Spin	102–167	**166.67**	**0.655**	1.10	**0.63**	**4.56×10^{-4}**

The bolded numbers refer to the optimal found design parameters for achieving high solar cell efficiency based on the selected photoanode and coating method.

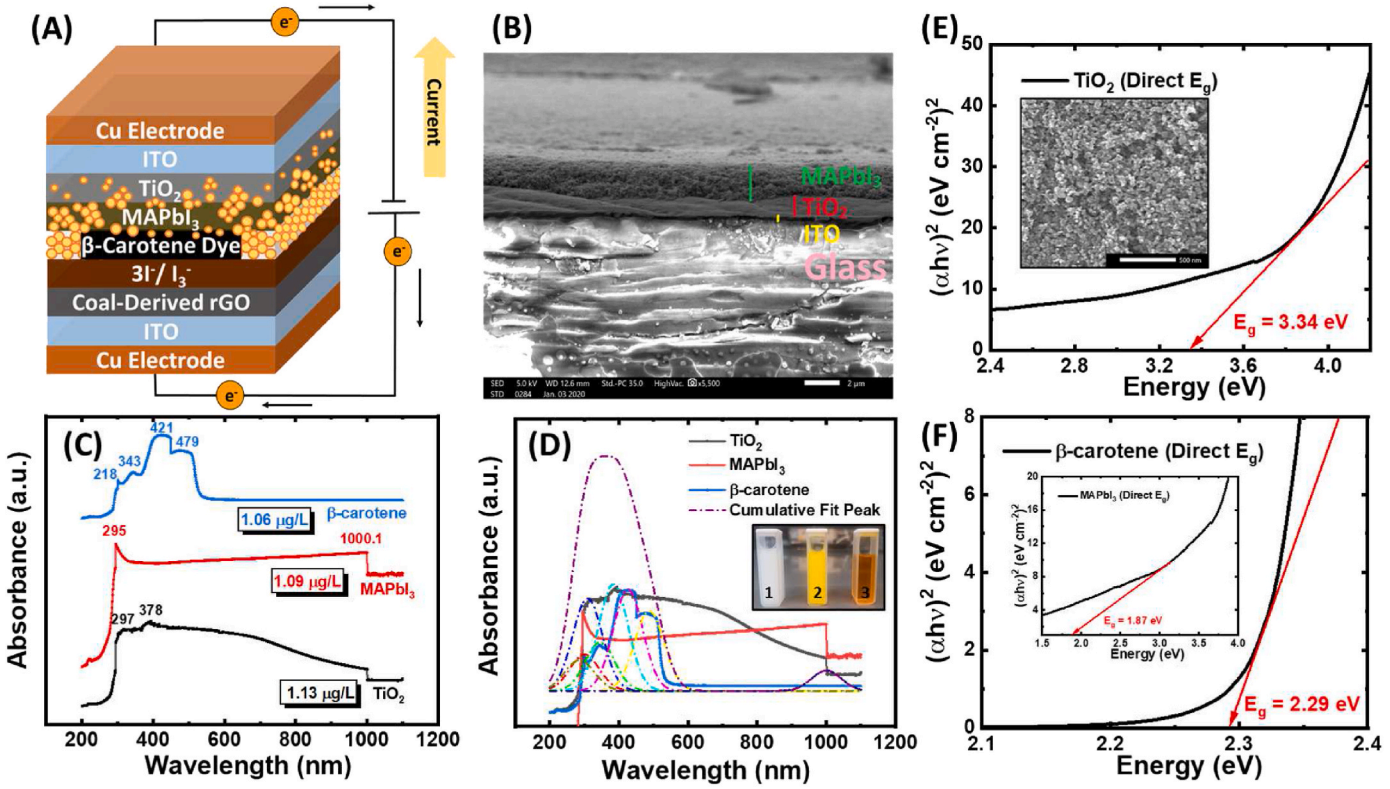

Fig. 4. β-carotene-sensitized and $MAPbI_3$-cosensitized bio-DSSCs: **(A)** Cartoon design of the DSSC with both β-carotene natural sensitizer and perovskite co-sensitizer; **(B)** FESEM image showing sensitized/cosensitized spin-coated photoanode cross section and deposited layers with their approximated thicknesses**; (C)** Absorbance curves for TiO_2 and sensitizers in H_2O solutions showing absorbance maximum of each material; **(D)** Cumulative peaks Gaussian fitting of the sub-fitted peaks of TiO_2 and sensitizers showing 2-fold increase in the photoanode light absorption within 200–600 nm UV–Vis spectrum, **inset of (D):** Solutions of (1) TiO_2, (2) $MAPbI_3$, and (3) β-carotene; **(E)** Tauc plot for TiO_2 semiconductor with direct bandgap = 3.34 eV, **inset of (E):** surface morphology of ITO/TiO_2 showing TiO_2 nanoparticles with average-diameter of 30–40 nm; **(F)** Tauc plot and direct bandgap for β-carotene (2.29 eV), **inset of (F):** Tauc plot and direct bandgap for $MAPbI_3$ (1.87 eV) sensitizers.

and the liquid electrolyte, which can easily damage the perovskite structure from the introduced wetting of the surface *via* iodide/triiodide electrolyte. From a comparison of our work with previous studies (2018–2020) [6,9,21,47,49,50] which utilized β-carotene in TiO_2-based DSSCs, none of the previous studies have been able to achieve V_{oc}>0.5 V, but with higher photocurrent densities than those observed here in the designed perovskite-cosensitized bio-DSSCs. This can be attributed to the role of $MAPbI_3$ in reducing the voltage loss from the presumed upward shifting in TiO_2 Fermi level (E_F) due to the increased number of injected electrons *via* $MAPbI_3$ cosensitization, resulting from the decreased φ_{SBH} at ITO/TiO_2 junction blocking back-electron transport. However, the observed low current densities may be a result of poor electron collection abilities of the GO/rGO-based CEs to capture the incoming forward electrons from the photoanode side. Thus, utilizing Ag might allow to increase the photocurrent density and achieve high PCEs.

The J-V curves of the architecturally designed DSSCs with different photoanodes are plotted in Fig. 3-C, with the obtained photovoltaic parameters and cell performance reported in Table 2. The involvement of both $MAPbI_3$ + β-carotene as a co-sensitizer and a sensitizer, respectively, resulted in increasing both J_{sc} and V_{oc} leading to a higher fill factor (FF) and PCE (η). The reason behind the enhanced voltage is attributed to the presumed upward shifting in TiO_2 Fermi level (E_F) due to the increased number of injected electrons *via* $MAPbI_3$ cosensitization (lower TiO_2 work function decreases φ_{SBH} at ITO/TiO_2 junction blocking back-electron transport for minimized voltage loss). Spin-coated photoanodes showed higher V_{oc} due to the reduced R_s and enhanced tunneling decreasing voltage loss based on the proposed transport mechanisms. However, the high currents in perovskites-sensitized cells are attributed to (i) low J_0 or less leakage current, (ii) enhanced exciton generation (e-h pairs) by the dye/perovskite molecules, and (iii) facilitated electron injection or charge separation at [$MAPbI_3$+dye]/TiO_2. Cosensitization with $MAPbI_3$ resulted in higher J_{sc} owing to the low R_s allowing easy e^- injection from enhanced exciton generations and photon absorption. Reproducibility of the J-V curves has been also considered (see Supplementary, Figure S3). The FF values of non-sensitized photoanode-based DSSCs are found low because FF is known to be associated with both V_{oc} and I_{sc} as well as the squareness of the J-V curve. Such low produced voltages have resulted in low FF∼ 0.3–0.6 due to the high current leakage and poor current collection from the undesired interfacial recombination introduced by added interfaces. FF values have increased from 0.24 to 0.36 and from 0.32 to 0.63 when TiO_2 nanoparticles were interfaced with [$MAPbI_3$ + β-carotene] using dip-coated and spin-coated (Fig. 3-D) photoanodes, respectively, in the different designed cell architectures (Figure S4). This results into a maximum PCE of (1.40–4.56) × 10^{-4}% (three-order-of-magnitudes higher than that of non-sensitized DSSCs, and 4-fold higher than similar β-carotene powder-based DSSCs [15]; see Table 3).

Series resistance (R_s) and shunt resistance (R_{sh}) were estimated from the linear relations obtained from the dark diode curves using Cheung's methods [68,69] equation: $\frac{dV}{d\ln(I)} = IR_s + \left(\frac{nk_BT}{q}\right)$, and the J-V curves as $R_s = -[\Delta V_{oc}/\Delta I_{oc}]$ and $R_{sh} = -[\Delta V_{sc}/\Delta I_{sc}]$, respectively, where $I = J$ here [70]. From the J-V curves, maximum power points were determined and taken as a reference to obtain the two linear lines at V_{oc} and J_{sc} locations. For efficient cells and high currents, R_s should be low for better electron injection and R_{sh} must be high enough to prevent current leakage. Both [$MAPbI_3$+β-carotene] enhanced R_{sh} (but with increased

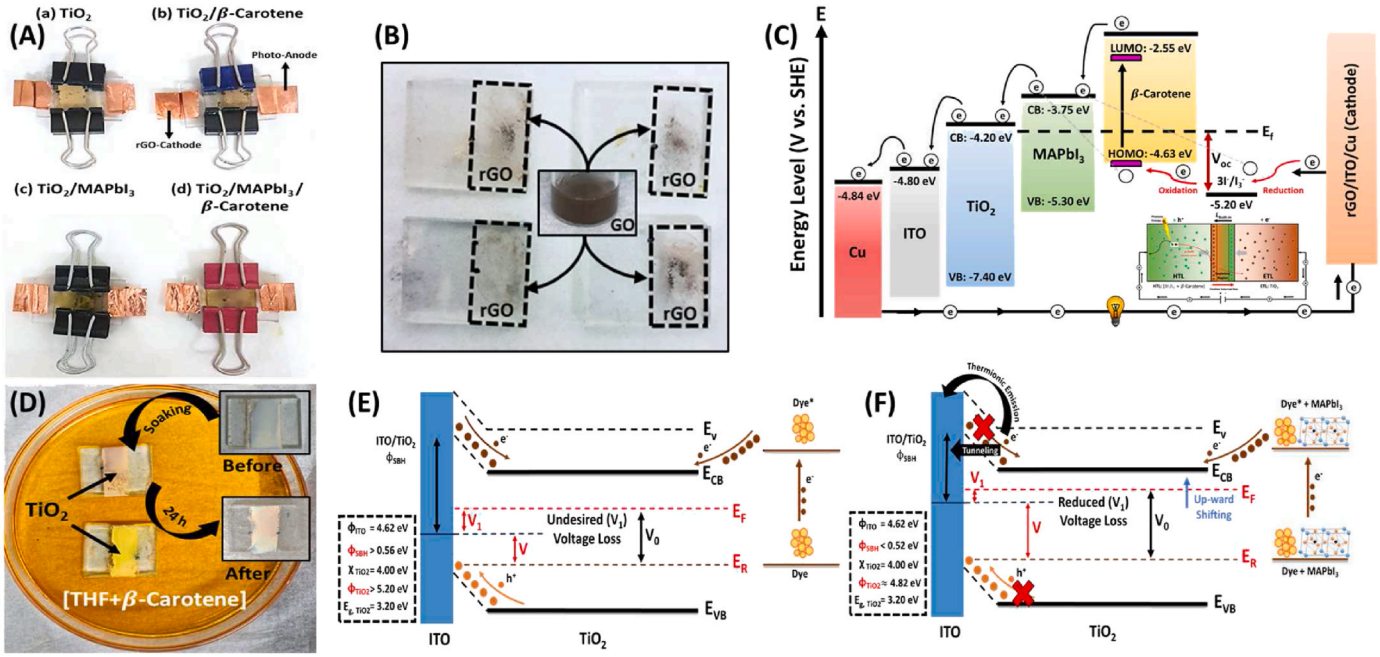

Fig. 5. **(A)** Fabricated bio-DSSCs using different photoanode designs with natural-sensitization and/or cosensitization; **(B)** Post-annealed ITO/rGO counter electrodes for lower R_s and efficient current (electron) collection; **(C)** Energy levels and band diagram alignment for the sensitized/cosensitized photoanode with perfect energy cascading for enhanced carriers mobility and lower interfacial recombination owing to the visible light absorption and low bandgaps of β-carotene and $MAPbI_3$, **inset of (C):** hypothesized HTL/ETL (or HTL/Perovskite/ETL) theory for exciton generation and charge transport across the built-in potential; **(D)** Crystallized TiO_2 dip-coated thin-film (2 cm × 1.5 cm) on ITO substrate before and after β-carotene overnight deposition/soaking; **(E)** TiO_2 Fermi level and ITO/TiO_2 SBH before $MAPbI_3$ cosensitization; **(F)** Upward shifting of TiO_2 Fermi level after $MAPbI_3$ cosensitization minimizing ITO/TiO_2 SBH for reduced voltage loss (V_1) and prevented back-electron transport to TiO_2.

R_s) yielding in relatively high RF and J_{sc} (Fig. 3-F). V_{oc} has been improved from the noticeable decrease in Φ_{SBH} at ITO/TiO_2 interface (from 0.61 to 0.53 eV) from addition of both [$MAPbI_3$ + β-carotene] sensitizers which prevented back-electron transport, and increased excitons generation and electron injection rates (Table 1). The sensitized/cosensitized photoanode active layers and cell architecture including β-carotene are illustrated in Fig. 4-A (Supplementary, see Figure S4 for the other designs).

The optimally designed cell structures with perovskite cosensitization are illustrated in Fig. 4-A. FESEM and SEM images (Fig. 4-B, Fig. 4-E inset, Figures S5-S8, EDS Figures S9, S10) show the uniformly deposited/annealed TiO_2 morphology on ITO and photoanode cross-section layers characterization for quantifying each layer thickness: ITO∼ 260 nm, TiO_2∼ 1.2 μm, and $MAPbI_3$∼ 2 μm. Since the annealing temperature of TiO_2 films was at 400 °C, anatase crystals are expected to form (300–700 °C) [71] (observed as small and scattered crystals with typical ∼ 40 nm grains), rather than rutile and brookite. Tauc plots for the WBG semiconductor and the sensitizers (Fig. 4-E and Fig. 4-F), obtained from UV–Vis absorbance curves (Fig. 4-C) and the linearized Tauc Equation $\alpha h\nu = A(h\nu - E_g)^{1/2}$ [72], are used to fit the absorption spectrum for the direct allowed transition bandgaps of TiO_2, $MAPbI_3$, and β-carotene. Despite that $MAPbI_3$ is considered a direct bandgap semiconductor due to the high VB density of state, an indirect bandgap exists from spin-orbit coupling owing to CB Rashba-splitting [73]; where α is the absorption coefficient, hv is the photon energy, A is a constant, and E_g is the bandgap; α is calculated from: $\alpha = (2.303t)^{*}OD$ where t is the thickness of the quartz cuvette (light path), 2.303 is the conversion constant between log(x) and ln(x) and OD is the optical density (UV/Vis absorbance) [73].

First-principle DFT calculations showed that anatase behaves as an indirect transition bandgap semiconductor with high photocatalytic activity. Indirect transition ensures a longer photogenerated exciton lifetime. Anatase phase of TiO_2 is characterized with the lightest average effective mass phase yielding faster electron migration from TiO_2 to ITO with minimum recombination rates within TiO_2 [74]. WBG TiO_2 was observed with a direct bandgap of 3.34 eV (Fig. 4-E) that is equivalent to the reported 3.3 eV for TiO_2 nanoparticles utilized by Kumar et al. [75] in naturally-sensitized DSSCs [Jambolana + Eosin dye] with 0.13% PCE, where absorbance lies in the UV region. The direct bandgap of $MAPbI_3$ was found to be 1.87 eV (inset in Fig. 4-F), which agrees with the Guo et al. [76] reported literature range (1.53–2.1 eV). An estimated direct bandgap of 2.29 eV (Fig. 4-F) was obtained for β-carotene; this is smaller than the maximum reported direct bandgap of 3.74 eV (1.59 eV for indirect transition) for β-carotene in the fabricated x (SnO_2)-y (Ag)-β-carotene/ITO photoanode [5,77]. However, other works estimated the HOMO/LUMO energy difference for various classes of carotene to be 2.2–6.7 eV [78]. Tunability of β-carotene's energy bandgap is possible *via* incorporation of Ag/SnO_2 nanoparticles yielding β-carotene nanocomposite with lower E_g for its application in DSSCs, giving better molecular-dye electron excitation [77]. Regarding tunablity of bandgap energy in TiO_2, increasing the semiconductor annealing temperature can blue-shift energies (decreasing bandgap); while, a decrease in semiconductor grain size decreases E_g due to electron quantum confinement [79].

Absorbance curves from Fig. 4-C showed maximum absorption (λ_{max}) for TiO_2 at 297, 378 cm^{-1}, $MAPbI_3$ at 295, 1000.1 cm^{-1}, and β-carotene at 218, 343, 421, 479 cm^{-1} confirming that TiO_2 absorbs light mostly from the UV-region whereas sensitization fosters visible-light absorption. Cumulative peaks fitting (Gaussian fitting in ORIGIN, Fig. 4-D) from the sub-fitted peaks of TiO_2 and both β-carotene and $MAPbI_3$ sensitizers confirmed a minimum of 2-fold increase in the photoanode light absorption capabilities in the 200–600 nm UV–Vis spectrum.

Maximum theoretical PCE of <0.1% (spin-coated) and <0.7% (dip-coated) are estimated from the maximum theoretical V_{oc} = 1 V plugged into [$V_{oc} = \frac{nk_BT}{q}\ln\left(\frac{J_{ph}}{J_0}\right)$] and [$\eta^{*} = \frac{P_m}{P_{in}}$] according to DSSCs circuit and TE models (Supplementary, see section 1) with an assumption that there

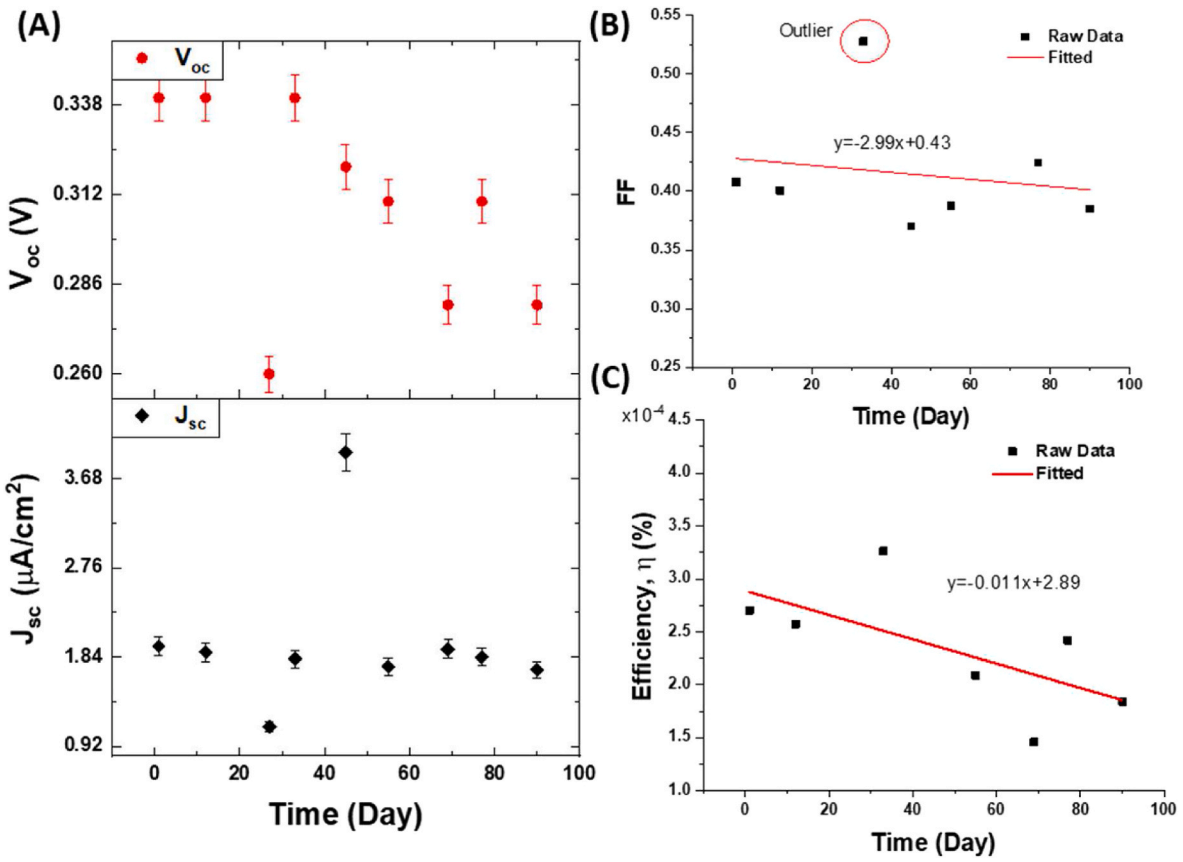

Fig. 6. Cell stability over time for naturally-sensitized bio-DSSCs using β-carotene dip-coated photoanodes: **(A)** Changes in the observed V_{oc} (2% error bars) and J_{sc} (5% error bars); **(B)** Slight reductions in FF with the estimated linear fitted relationship considering an outlier value; **(C)** Slight reductions in efficiency with the estimated linear fitted relationship after removing any outlier values.

will be similar observed current densities; where symbols definitions can be found in the Supplementary, see section 1. If current densities rise $\times$100 from using a silver (Ag) counter electrode, the maximum PCE can then theoretically go up to $\approx$10%.

The β-carotene dye deposited on TiO_2-photoanodes and their use in the different designed/fabricated DSSCs are shown in Fig. 5-D and Fig. 5-A, respectively. Post-annealed and prepared ITO/rGO CEs for lower R_s are shown in Fig. 5-B. The uniformity of the rGO film determines the capability of the CE for current collection; however, the random deposition and non-uniform coated rGO negatively influenced the device performance by sharply decreasing J_{sc} to $\sim \mu A/cm^2$. Such uniform coating of graphite-based materials is mandatory for easy electron collection and enhanced current density. Energy band diagram alignment in Fig. 5-C illustrates perfect energy cascading for enhanced photoanode electron mobility, reduced interfacial recombination, and continuous forward electron pathways. The low bandgaps of both β-carotene (2.29 eV) and $MAPbI_3$ (1.87 eV) assure visible-light absorption, with their LUMO ($-$2.55 eV) and CB ($-$3.75 eV) relatively in higher states than TiO_2 CB ($-$4.2 eV) for more exciton generation and easy electron injection with a maximum ideal $V_{oc} = 1$ V. The shift in the bandgap of $MAPbI_3$ crystals from known bandgap around 1.6 eV–1.87 eV might be attributed to the decomposition of perovskites when interfaced with the liquid redox electrolyte [I^-/I_3^-]. Low electron excitation energy requirements in the sensitizers ensure easy electron excitation and injection above the Fermi level of TiO_2. The large difference between HOMO/redox potentials drives electron-diffusion which effectively controls the charge injection and dye reduction rates [80].

In DSSCs, a Schottky diode exists at the metal-semiconductor interface in the photoanode structure as in ITO/TiO_2 or [Cu/ITO]/TiO_2 junctions. Onodera et al. showed that V_{oc} decreased with increasing φ_{SBH} [40–42]. When TiO_2 comes in contact with ITO, band bending in TiO_2 CB occurs influencing the current-loss mechanism from inhibited electron collection or increased recombination in agreement with the thermionic-emission theory [42]. We suspect that there are three mechanisms responsible for the improved PCE from $MAPbI_3$ cosensitization: (i) absorbance broadening and increase in the probability of absorbing more visible-photons (400–700 nm) [35], (ii) upward shifting of TiO_2 Fermi level due to increased injected electrons and CB effective density of states $>2.46 \times 10^{21}$ cm^{-3} reducing the TiO_2 work function to 4.82 eV (Supplementary, seesection 9), consequently preventing back-electron transport allowing only quantum tunneling of photoelectrons at ITO/TiO_2, rather than transport over a Schottky barrier [81, 82] (Fig. 5-E,F), and (iii) hindered φ_{SBH} at the ITO/TiO_2 interface with a 13.1% reduction in photoinduced electrostatic potential barrier due to the minimized band bending of TiO_2 CB and reduced TiO_2 work function resulting in low built-in potential and lower voltage loss (V_1). All of the described mechanisms are attributed to possible ITO/TiO_2 electron tunneling from the increased number of initially injected electrons from perovskite and dye molecules into TiO_2 CB [42,83]. Briefly, this upward shifting in E_F level for TiO_2 promotes both electron tunneling and V_{oc} while decreasing the minimum TiO_2 work function (φ_{TiO_2}) required for electron excitation, injected electrons tunnel from TiO_2 to ITO overcoming the suppressed φ_{SBH} at the presumed junction with hindered TiO_2 CB band bending resulting in less recombination and high V_{oc} [84–86] from the $MAPbI_3$ cosensitization.

The stability of the designed devices and photoanodes have been studied over time (3-month period) as shown in Fig. 6. This would allow us to study the durability of utilizing perovskite semiconductors to cosensitize naturally-sensitized bio-DSSCs. The long-term stability of the devices is a critical indicator to assess the practicability and operability

Table 3
Performance comparison and photovoltaic parameters of various literature works on β-carotene-based DSSCs in contrast with the proposed bio-DSSCs system under AM1.5G radiation.*

Pigment: Source/Absorbance | [Architecture]	J_{sc} (μA cm^{-2})	V_{oc} (mV)	FF	η^* (%)	Ref.
Daucus Carota/415–508 nm [FTO/TiO_2/β-carotene/[I^-/I_3^-]/C/FTO]	33	239	–	1.2×10^{-3}	[39]
Carrot/400–510 nm; peaks: 433, 472.5 nm [FTO/TiO_2/β-carotene/[I^-/I_3^-]/Pt/FTO]	360	40	0.64	9×10^{-3}	[21]
Orange fruit; 400–510 nm; peaks: 441, 466.5 nm [FTO/TiO_2/β-carotene/[I^-/I_3^-]/Pt/FTO]	370	60	0.58	2×10^{-2}	[21]
Tomatoes/400–510 nm; max: 441 nm and 466.5 nm [FTO/TiO_2/β-carotene/[I^-/I_3^-]/Pt/FTO]	510	140	0.37	3×10^{-2}	[21]
Syngonium sp leafs/440–480 nm; peaks: 450, 480 nm; bandgap = 2.47 eV; EL-HSE (High stability redox, Dyesol) [FTO/TiO_2/β-carotene/[I^-/I_3^-]/Pt/FTO]	270	400	0.68	7.4×10^{-2}	[9]
Yellow sweet potato/400–500 nm; peaks: 401 nm [FTO/TiO_2/β-carotene/[I^-/I_3^-]/Pt/FTO]	0.27	515	–	5.7×10^{-2}	[6]
Purple sweet potato/400–500 nm; peaks: 532 nm, [FTO/TiO_2/β-carotene/[I^-/I_3^-]/Pt/FTO]	0.17	378	–	3.3×10^{-2}	[6]
β-carotene powder; 380–500 nm [ITO/TiO_2/β-carotene/[I^-/I_3^-]/C/ITO]	162	123	0.039	1×10^{-4}	[50]
β-carotene powder; 218–479 nm [ITO/TiO_2/$MAPbI_3$/β-carotene/[I^-/I_3^-]/rGO/ITO]	1.10	655	0.63	4.6×10^{-4}	This work

*J_{sc} = Short-circuit current density; V_{oc} = Open-circuit voltage; FF = Fill factor; η = Incident photon-to-current efficiency (IPCE) = Quantum efficiency (QE). Note that we have used the β-carotene powder source similar to the last reported study [50], Sigma US, and recorded better η.

of such naturally-sensitized devices simply assembled under ambient conditions. Both FF and J_{sc} values found to be almost the same over 3 months, as illustrated in Fig. 6-A and Fig. 6-B. This indicates the capability of the deposited light-absorbing layers in maintaining forward electron transport and charge separation. It is worth mentioning that each of the nine measurements was carried under a light incident of 100 mW/cm^2 with three values averaged over a 2 h radiation period with surrounding humidity ~ 35%, and room temperature of ~ 23 °C. The stable current generation (even at low values) suggests a stable photoanode layer and stable electron collection at the cathode side. However, the overall PCE decrease rate was found to be 10%/month, which is due to the poor stability of $MAPbI_3$ for maintaining high V_{oc} based on the suggested transport mechanisms and the hindered loss of voltage from SBH, as obtained in Fig. 6-A and Fig. 6-C. In other words, the observed low voltage is linked to possible degradation of the $MAPbI_3$ layer from excess oxygen and light stresses. Also, $MAPbI_3$ crystals are more susceptible to degrade and lose their octahedral stable structures when coming in contact with a liquid-state electrolyte, resulting in decreasing both V_{oc} and device efficiency over time.

Apparently, employing environmental-friendly sensitizers including biomolecular dyes (carotenoids) with perovskite semiconductors for hybrid photoanode architectures will facilitate exciton generation and electron forward transport owing to the highly conjugated dye double bonds structure (π-electrons in their molecular structure) [12,13,87] and broadened UV–Vis absorption. The designed solar cells are of a conventional type where electrons move to n-type (ETL) and hole to p-type (HTL) layers ensuring fast charge separation. Both $MAPbI_3$ and β-carotene absorb incident photons which initiate electron excitation before the charge separation step. Further photoelectrochemical characterizations such as EIS, IPCE, IMVS, and IMPS are important to essentially understand the proposed mechanisms and the reasons behind the low current and/or reduced cell efficiency. Future works and further steps may include the following: (i) utilization of acidic dye solutions and/or surface hydroxylation of TiO_2 semiconductor (to introduce more –OH anchoring groups) for strong dye molecules acceptor-moieties attachment yielding in lower series resistance, (ii) designing of 3D graphene-based counter electrodes with interconnected networks to provide fast electron transport from the cathode, diminished contact resistance at the graphene/electrolyte interface [88], and high electrocatalytic activity towards reduction of I_3^-, and (iii) incorporation of low-dimensional WBG 1D-ZnO nanowires ensuring large surface area for better dye coverage, high V_{oc}, and enhanced photoanode stability against excessive UV radiation. Table 3 shows a performance comparison of β-carotene-based DSSCs with previous recent works (2018–2020) [6,9,21,47,49,50], as have been earlier discussed in the second section of this work.

5. Conclusion

We demonstrated natural photosensitization using bio-sensitized TiO_2 photoanodes which are further cosensitized by $MAPbI_3$ perovskite semiconductors for enhanced photon absorption, exciton generation, charge separation, and electron injection resulting in reduced voltage loss. The hybrid biomolecular dye-perovskite photoanode heterostructure [TiO_2/$MAPbI_3$/β-carotene] can broaden the optical absorption spectrum and reduce interfacial recombination, and most importantly facilitate interfacial charge separation, electron injection, and electron tunneling which reduce voltage loss at the presumed ITO/TiO_2 heterojunction for enhanced V_{oc}. The observed results were attributed to the perovskite engineered cascaded molecular energy levels in the hybrid biophotonode, which enabled upward shifting in Fermi level (E_F) for TiO_2, reduced work function in TiO_2, that would hinder TiO_2 CB bending. Perovskite semiconductor-integrated biophotoanode structures found to enhance the diode ideality factor, reduce the leakage current, improve the cell rectification factors, increase the FF, and noticeably show high V_{oc} (>0.65 V), from shifting of E_F level and lowering of φ_{SBH}.

The use of β-carotene as a light-absorbing material instead of the Ru-based complexes is already known to result in DSSCs with low PCEs, which can be further improved *via* perovskite semiconductor cosensitization. The thickness of the β-carotene and the number of absorbed photons in the dye layer needs to be further investigated for understanding the charge transport mechanisms and quantifying carrier lifetime. The very low device efficiency (in the order of 10^{-2}–10^{-4}%) might be attributed to the poor devices stability and degradation of $MAPbI_3$ layers when interfaced with the liquid electrolyte [I^-/I_3^-]. The designed solar cells are of a conventional type where electrons transport to n-type (ETL) and holes to p-type (HTL) layers ensuring fast charge separation. Both $MAPbI_3$ and β-carotene absorb incident photons which initiate electron excitation before the charge separation step. Further photoelectrochemical characterizations such as EIS, IPCE, IMVS, and IMPS are important to essentially understand the proposed mechanisms and the reasons behind the low photocurrent and/or cell efficiency. The low photocurrent densities could be due to the unfavorable high series resistances that need further investigation on the engineered interfacial contacts with the possibility of using Ag and/or noble-Pt-like CE for better electron collection. Nevertheless, cosensitization prevents back-electron transport which also facilitates exciton generation, electron injection, and the possibility of a 2-fold increase in photoanode UV–Vis absorption capabilities. This work paves the way towards designing efficient bio/co-sensitized photoanodes, which can be further improved

from the incorporation of WBG low-dimensional materials, solid-state HTL redox electrolytes, and Ag/Au plasmonic nanoparticles leveraging photon absorption, electron injection and hopping, dye regeneration, and interfacial charge transport for improved overall device performance.

Credit author statement

Hisham A. Maddah: Conceptualization; Data curation; Formal analysis; Investigation; Methodology; Resources; Visualization; Roles/Writing - original draft; Writing – review & editing. **Lila Aryadwita**: Formal analysis; Investigation; Writing – review & editing. **Vikas Berry**: Resources; Supervision; Writing – review & editing. **Sanjay K. Behura**: Conceptualization; Investigation; Data curation; Formal analysis; Methodology; Project administration; Resources; Supervision; Visualization; Roles/Writing - original draft; Writing – review & editing

Declaration of competing interest

The authors declare that they have no known competing financial interests or personal relationships that could have appeared to influence the work reported in this paper.

Acknowledgements

SKB and VB thank Dimerond Technologies, LLC for the support to conduct renewable energy research at the University of Illinois at Chicago. All the authors thank University of Illinois at Chicago for the support. SKB thank Dr. Qinglong Jiang for the scientific discussion. SKB thank University of Arkansas at Pine Bluff for the support. HAM would like to acknowledge the Saudi Arabian Cultural Mission (SACM) for their funding to pursue graduate studies and Deanship of Scientific Research (DSR) at King Abdulaziz University (KAU) for their support and motivation. The authors wish to thank Charles Atkins and Garrett Lindemann from Ramaco Carbon for the collaboration and for providing the coal samples. VB thanks funding support from National Science Foundation (grant: 1054877) and Office of Naval Research (grants: N000141110767 and N000141812583).

Appendix A. Supplementary data

Supplementary data to this article can be found online at https://doi.org/10.1016/j.rser.2021.111606.

References

[1] Hagfeldt A. Brief overview of dye-sensitized solar cells. Ambio 2012. https://doi.org/10.1007/s13280-012-0272-7.
[2] Sugathan V, John E, Sudhakar K. Recent improvements in dye sensitized solar cells: a review. Renew Sustain Energy Rev 2015. https://doi.org/10.1016/j.rser.2015.07.076.
[3] Parida B, Iniyan S, Goic R. A review of solar photovoltaic technologies. Renew Sustain Energy Rev 2011. https://doi.org/10.1016/j.rser.2010.11.032.
[4] Sawhney N, Raghav A, Satapathi S. Utilization of naturally occurring dyes as sensitizers in dye sensitized solar cells. IEEE J Photovoltaics 2017. https://doi.org/10.1109/JPHOTOV.2016.2639343.
[5] Maddah HA, Berry V, Behura SK. Biomolecular photosensitizers for dye-sensitized solar cells: recent developments and critical insights. Renew Sustain Energy Rev 2020. https://doi.org/10.1016/j.rser.2019.109678.
[6] Cari C, Khairuddin K, Septiawan TY, Suciatmoko PM, Kurniawan D, Supriyanto A. The preparation of natural dye for dye-sensitized solar cell (DSSC). AIP Conf. Proc. 2018. https://doi.org/10.1063/1.5054510.
[7] Mathew S, Yella A, Gao P, Humphry-Baker R, Curchod BFE, Ashari-Astani N, et al. Dye-sensitized solar cells with 13% efficiency achieved through the molecular engineering of porphyrin sensitizers. Nat Chem 2014. https://doi.org/10.1038/nchem.1861.
[8] Hao S, Wu J, Huang Y, Lin J. Natural dyes as photosensitizers for dye-sensitized solar cell. Sol Energy 2006. https://doi.org/10.1016/j.solener.2005.05.009.
[9] Nirwana Sari Halidun WO, Cahya Prima E, Yuliarto B, Suyatman. Fabrication dye sensitized solar cells (DSSCs) using β-carotene pigment based natural dye. MATEC Web Conf. 2018. https://doi.org/10.1051/matecconf/201815902052.
[10] Srivastava SK, Piwek P, Ayakar SR, Bonakdarpour A, Wilkinson DP, Yadav VG. A biogenic Photovoltaic Material. Small. 2018. https://doi.org/10.1002/smll.201800729.
[11] Hug H, Bader M, Mair P, Glatzel T. Biophotovoltaics: natural pigments in dye-sensitized solar cells. Appl Energy 2014. https://doi.org/10.1016/j.apenergy.2013.10.055.
[12] Nagai A, Takagi K. Conjugated Objects: Developments, Synthesis, and Applications. Pan Stanford; 2017.
[13] Samal A. Brief Discussion on Color: Why does such conjugation allow absorption of visible light?. 2014. https://people.chem.umass.edu/samal/269/color.pdf.
[14] Wu CY, Tu KJ, Deng JP, Lo YS, Wu CH. Markedly enhanced surface hydroxyl groups of TiO2 nanoparticles with superior water-dispersibility for photocatalysis. Materials 2017. https://doi.org/10.3390/ma10050566.
[15] Du Y, Petrik NG, Deskins NA, Wang Z, Henderson MA, Kimmel GA, et al. Hydrogen reactivity on highly-hydroxylated TiO2(110) surfaces prepared via carboxylic acid adsorption and photolysis. Phys Chem Chem Phys 2012. https://doi.org/10.1039/c1cp22515d.
[16] Zhang D, Yang M, Dong S. Hydroxylation of the rutile TiO2(110) surface enhancing its reducing power for photocatalysis. J Phys Chem C 2015. https://doi.org/10.1021/jp510427v.
[17] Kojima A, Teshima K, Shirai Y, Miyasaka T. Organometal halide perovskites as visible-light sensitizers for photovoltaic cells. J Am Chem Soc 2009. https://doi.org/10.1021/ja809598r.
[18] Im JH, Lee CR, Lee JW, Park SW, Park NG. 6.5% efficient perovskite quantum-dot-sensitized solar cell. Nanoscale 2011. https://doi.org/10.1039/c1nr10867k.
[19] Kakiage K, Kyomen T, Hanaya M. Improvement in photovoltaic performance of dye-sensitized solar cells by cosensitization with an organometal halide perovskite. Chem Lett 2013. https://doi.org/10.1246/cl.130774.
[20] Kim HS, Lee JW, Yantara N, Boix PP, Kulkarni SA, Mhaisalkar S, et al. High efficiency solid-state sensitized solar cell-based on submicrometer rutile TiO2 nanorod and CH3NH3PbI3 perovskite sensitizer. Nano Lett 2013. https://doi.org/10.1021/nl400286w.
[21] Supriyanto A, Nurosyid F, Ahliha AH. Carotenoid pigment as sensitizers for applications of dye-sensitized solar cell (DSSC). IOP Conf Ser Mater Sci Eng 2018. https://doi.org/10.1088/1757-899X/432/1/012060.
[22] Musyaro'Ah Huda I, Indayani W, Gunawan B, Yudhoyono G, Endarko. Fabrication and characterization dye sensitized solar cell (DSSC) based on TiO2/SnO2 composite. AIP Conf. Proc. 2017. https://doi.org/10.1063/1.4968315.
[23] Rani M, Tripathi SK. A comparative study of nanostructured TiO2, ZnO and bilayer TiO2/ZnO dye-sensitized solar cells. J Electron Mater 2015. https://doi.org/10.1007/s11664-015-3636-5.
[24] Zhou Y, Xia C, Hu X, Huang W, Aref AA, Wang B, et al. Dye-sensitized solar cells based on nanoparticle-decorated ZnO/SnO2 core/shell nanoneedle arrays. Appl Surf Sci 2014. https://doi.org/10.1016/j.apsusc.2013.11.095.
[25] Zhang W, Eperon GE, Snaith HJ. Metal halide perovskites for energy applications. Nat Energy 2016. https://doi.org/10.1038/nenergy.2016.48.
[26] Maddah HA, Berry V, Behura SK. Cuboctahedral stability in Titanium halide perovskites via machine learning. Comput Mater Sci 2020. https://doi.org/10.1016/j.commatsci.2019.109415.
[27] Park NG. Perovskite solar cells: an emerging photovoltaic technology. Mater Today 2015. https://doi.org/10.1016/j.mattod.2014.07.007.
[28] Tzounis L, Stergiopoulos T, Zachariadis A, Gravalidis C. ScienceDirect Perovskite solar cells from small scale spin coating process towards roll-to-roll printing : optical and Morphological studies. Mater Today Proc 2017;4:5082–9. https://doi.org/10.1016/j.matpr.2017.04.117.
[29] Motta C, El-Mellouhi F, Sanvito S. Charge carrier mobility in hybrid halide perovskites. Sci Rep 2015. https://doi.org/10.1038/srep12746.
[30] Ning W, Wang F, Wu B, Lu J, Yan Z, Liu X, et al. Long electron–hole diffusion length in high-quality lead-free double perovskite films. Adv Mater 2018. https://doi.org/10.1002/adma.201706246.
[31] Edri E, Kirmayer S, Cahen D, Hodes G. High open-circuit voltage solar cells based on organic-inorganic lead bromide perovskite. J Phys Chem Lett 2013. https://doi.org/10.1021/jz400348q.
[32] Kim HS, Lee CR, Im JH, Lee KB, Moehl T, Marchioro A, et al. Lead iodide perovskite sensitized all-solid-state submicron thin film mesoscopic solar cell with efficiency exceeding 9%. Sci Rep 2012. https://doi.org/10.1007/s10340-012-0467-5.
[33] Ye S, Sun W, Li Y, Yan W, Peng H, Bian Z, et al. CuSCN-based inverted planar perovskite solar cell with an average PCE of 15.6%. Nano Lett 2015. https://doi.org/10.1021/acs.nanolett.5b00116.
[34] Behura SK, Wang C, Wen Y, Berry V. Graphene–semiconductor heterojunction sheds light on emerging photovoltaics. Nat Photonics 2019. https://doi.org/10.1038/s41566-019-0391-9.
[35] Grätzel M. Conversion of sunlight to electric power by nanocrystalline dye-sensitized solar cells. J Photochem Photobiol Chem 2004. https://doi.org/10.1016/j.jphotochem.2004.02.023.
[36] Maddah HA. Modeling and designing of a novel lab-scale passive solar still. J Eng Technol Sci 2019. https://doi.org/10.5614/j.eng.technol.sci.2019.51.3.1.
[37] Órdenes-Aenishanslins N, Anziani-Ostuni G, Vargas-Reyes M, Alarcón J, Tello A, Pérez-Donoso JM. Pigments from UV-resistant antarctic bacteria as photosensitizers in dye sensitized solar cells. J Photochem Photobiol B Biol 2016. https://doi.org/10.1016/j.jphotobiol.2016.08.004.
[38] Wang XF, Fujii R, Ito S, Koyama Y, Yamano Y, Ito M, et al. Dye-sensitized solar cells using retinoic acid and carotenoic acids: dependence of performance on the conjugation length and the dye concentration. Chem Phys Lett 2005. https://doi.org/10.1016/j.cplett.2005.09.020.

[39] Suryana R, Khoiruddin Supriyanto A. Beta-carotene dye of daucus carota as sensitizer on dye-sensitized solar cell. Mater Sci Forum 2013. https://dx.doi.org/10.4028/www.scientific.net/MSF.737.15.

[40] Onodera M, Nagumo R, Miura R, Suzuki A, Tsuboi H, Hatakeyama N, et al. Multiscale simulation of dye-sensitized solar cells considering Schottky barrier effect at photoelectrode. Jpn J Appl Phys 2011. https://doi.org/10.1143/JJAP.50.04DP06.

[41] Nazeeruddin MK, Kay A, Rodicio I, Humphry-Baker R, Müller E, Liska P, et al. Conversion of light to electricity by cis-X2Bis (2,2′-bipyridyl-4,4′-dicarboxylate) ruthenium (II) charge-transfer sensitizers (X = Cl−, Br−, I−, CN−, and SCN−) on nanocrystalline TiO2Electrodes. J Am Chem Soc 1993. https://doi.org/10.1021/ja00067a063.

[42] Ni M, Leung MKH, Leung DYC, Sumathy K. Theoretical modeling of TiO2/TCO interfacial effect on dye-sensitized solar cell performance. Sol Energy Mater Sol Cells 2006. https://doi.org/10.1016/j.solmat.2006.02.005.

[43] Ananth S, Vivek P, Solaiyammal T, Murugakoothan P. Pre dye treated titanium dioxide nano particles sensitized by natural dye extracts of Pterocarpus marsupium for dye sensitized solar cells. Optik 2015. https://doi.org/10.1016/j.ijleo.2015.02.066.

[44] Marinado T. Photoelectrochemical studies of dye-sensitized solar cells using organic dyes. 2009.

[45] Gómez-Ortíz NM, Vázquez-Maldonado IA, Pérez-Espadas AR, Mena-Rejón GJ, Azamar-Barrios JA, Oskam G. Dye-sensitized solar cells with natural dyes extracted from achiote seeds. Sol Energy Mater Sol Cells 2010. https://doi.org/10.1016/j.solmat.2009.05.013.

[46] Long R, Fang WH, Prezhdo OV. Strong interaction at the perovskite/TiO2 interface facilitates ultrafast photoinduced charge separation: a nonadiabatic molecular dynamics study. J Phys Chem C 2017. https://doi.org/10.1021/acs.jpcc.6b12921.

[47] Zanjanchi F, Beheshtian J. Natural pigments in dye-sensitized solar cell (DSSC): a DFT-TDDFT study. J Iran Chem Soc 2019. https://doi.org/10.1007/s13738-018-1561-2.

[48] Pandey AK, Ahmad MS, Rahim NA, Tyagi VV, Saidur R. Natural sensitizers and their applications in dye-sensitized solar cell. Environ. Biotechnol. Sustain. Futur. 2018. https://doi.org/10.1007/978-981-10-7284-0_15.

[49] Tsao HN, Burschka J, Yi C, Kessler F, Nazeeruddin MK, Grätzel M. Influence of the interfacial charge-transfer resistance at the counter electrode in dye-sensitized solar cells employing cobalt redox shuttles. Energy Environ Sci 2011. https://doi.org/10.1039/c1ee02389f.

[50] Rangel D, Gallegos JC, Vargas S, García F, Rodríguez R. Optimized dye-sensitized solar cells: a comparative study with different dyes, mordants and construction parameters. Results Phys 2019. https://doi.org/10.1016/j.rinp.2019.01.096.

[51] Franck H, Cogdell RJ. In: Young A, Britt G, editors. Photochemistry and function of carotenoids in photosynthesis. Carotenoids Photosynth.; 1993.

[52] Koyama Y, Fujii R. Cis-trans carotenoids in photosynthesis: configurations, excited-state properties and physiological functions. In: Photochem. carotenoids. Dordrecht: Springer; 1999. p. 161–88.

[53] Frank HA, Brudvig GW. Redox functions of carotenoids in photosynthesis. Biochemistry 2004. https://doi.org/10.1021/bi0492096.

[54] Rani M, Tripathi SK. Electron transfer properties of organic dye sensitized ZnO and ZnO/TiO2 photoanode for dye sensitized solar cells. Renew Sustain Energy Rev 2016. https://doi.org/10.1016/j.rser.2016.03.012.

[55] Craft NE, Soares JH. Relative solubility, stability, and absorptivity of lutein and β-carotene in organic solvents. J Agric Food Chem 1992. https://doi.org/10.1021/jf00015a013.

[56] Zhou H, Wu L, Gao Y, Ma T. Dye-sensitized solar cells using 20 natural dyes as sensitizers. J Photochem Photobiol Chem 2011. https://doi.org/10.1016/j.jphotochem.2011.02.008.

[57] Hardcastle FD. Raman spectroscopy of titania (TiO2) nanotubular water-splitting catalysts. J Ark Acad Sci 2011;65.

[58] Hardcastle FD, Ishihara H, Sharma R, Biris AS. Photoelectroactivity and Raman spectroscopy of anodized titania (TiO2) photoactive water-splitting catalysts as a function of oxygen-annealing temperature. J Mater Chem 2011. https://doi.org/10.1039/c0jm03106b.

[59] Pérez-Osorio MA, Lin Q, Phillips RT, Milot RL, Herz LM, Johnston MB, et al. Raman spectrum of the organic-inorganic halide perovskite CH3NH3PbI3from first principles and high-resolution low-temperature Raman measurements. J Phys Chem C 2018. https://doi.org/10.1021/acs.jpcc.8b04669.

[60] Quarti C, Grancini G, Mosconi E, Bruno P, Ball JM, Lee MM, et al. The Raman spectrum of the CH3NH3PbI3 hybrid perovskite: interplay of theory and experiment. J Phys Chem Lett 2014. https://doi.org/10.1021/jz402589q.

[61] Thampy S, Zhang B, Hong K-H, Cho K, Hsu JWP. Altered stability and degradation pathway of CH3NH3PbI3 in contact with metal oxide. ACS Energy Lett 2020. https://doi.org/10.1021/acsenergylett.0c00041.

[62] Jehlička J, Edwards HGM, Oren A. Raman spectroscopy of microbial pigments. Appl Environ Microbiol 2014. https://doi.org/10.1128/AEM.00699-14.

[63] Tschirner N, Schenderlein M, Brose K, Schlodder E, Mroginski MA, Hildebrandt P, et al. Raman excitation profiles of β-carotene - novel insights into the nature of the ν1-band. Phys. Status Solidi Basic Res. 2008. https://doi.org/10.1002/pssb.200879649.

[64] Fang S, Huang D, Lv R, Bai Y, Huang ZH, Gu J, et al. Three-dimensional reduced graphene oxide powder for efficient microwave absorption in the S-band (2-4 GHz). RSC Adv 2017. https://doi.org/10.1039/c7ra03215c.

[65] Childres I, Jauregui LA, Park W, Cao H, Chen Y. Raman spectroscopy of graphene and related materials. New Dev Phot Mater Res 2013. https://doi.org/10.1016/B978-0-444-53175-9.00016-7.

[66] Gupta RK, Ghosh K, Kahol PK. Fabrication and electrical characterization of Au/p-Si/STO/Au contact. Curr Appl Phys 2009;9:933–6.

[67] Al-Hossainy AF, Zoromba MS, Abdel-Aziz MH, Bassyouni M, Attar A, Zwawi M, et al. Fabrication of heterojunction diode using doped-poly (ortho-aminophenol) for solar cells applications. Phys B Condens Matter 2019;566. https://doi.org/10.1016/j.physb.2019.04.030.

[68] Çavuş HK, Voigt MM, Şahingöz R. Optical and electrical properties of new organic thin film. J Mater Sci Mater Electron 2013. https://doi.org/10.1007/s10854-013-1483-9.

[69] Brutscher N, Hoheisel M. Schottky diodes with high series resistance: a simple method of determining the barrier heights. Solid State Electron 1988. https://doi.org/10.1016/0038-1101(88)90089-5.

[70] Diantoro M, Suprayogi T, Hidayat A, Taufiq A, Fuad A, Suryana R. Shockley's equation fit analyses for solar cell parameters from I-V curves. Int J Photoenergy 2018. https://doi.org/10.1155/2018/9214820.

[71] Nakaruk A, Ragazzon D, Sorrell CC. Anatase-rutile transformation through high-temperature annealing of titania films produced by ultrasonic spray pyrolysis. Thin Solid Films 2010. https://doi.org/10.1016/j.tsf.2009.10.109.

[72] Tauc J, Menth A. States in the gap. J Non-Cryst Solids 1972. https://doi.org/10.1016/0022-3093(72)90194-9.

[73] Wang T, Daiber B, Frost JM, Mann SA, Garnett EC, Walsh A, et al. Indirect to direct bandgap transition in methylammonium lead halide perovskite. Energy Environ Sci 2017. https://doi.org/10.1039/c6ee03474h.

[74] Zhang J, Zhou P, Liu J, Yu J. New understanding of the difference of photocatalytic activity among anatase, rutile and brookite TiO2. Phys Chem Chem Phys 2014. https://doi.org/10.1039/c4cp02201g.

[75] Ashok Kumar K, Manonmani J, Senthilselvan J. Effect on interfacial charge transfer resistance by hybrid co-sensitization in DSSC applications. J Mater Sci Mater Electron 2014. https://doi.org/10.1007/s10854-014-2304-5.

[76] Guo X, McCleese C, Kolodziej C, Samia ACS, Zhao Y, Burda C. Identification and characterization of the intermediate phase in hybrid organic-inorganic MAPbI3 perovskite. Dalton Trans 2016. https://doi.org/10.1039/c5dt04420k.

[77] Diantoro M, Sa'adah U, Hidayat A. Effect of SnO2 nanoparticles on band gap energy of x (SnO2)-y (Ag)-β-Carotene/FTO thin film. J Phys Conf Ser 2018;1093:012049.

[78] Martins JBL, Durães JA, Sales MJA, Vilela ASFA, Silva GME, Gargano R. Theoretical investigation of carotenoid ultraviolet spectra. Int J Quant Chem 2009. https://doi.org/10.1002/qua.21845.

[79] Tumuluri A, Lakshun Naidu K, James Raju KC. Band gap determination using Tauc's plot for LiNbO3 thin films. Int J Chem Res 2014.

[80] Calogero G, Yum JH, Sinopoli A, Di Marco G, Grätzel M, Nazeeruddin MK. Anthocyanins and betalains as light-harvesting pigments for dye-sensitized solar cells. Sol Energy 2012. https://doi.org/10.1016/j.solener.2012.02.018.

[81] Rühle S, Cahen D. Electron tunneling at the TiO2/substrate interface can determine dye-sensitized solar cell performance. J Phys Chem B 2004. https://doi.org/10.1021/jp047686s.

[82] Shiraishi Y, Yasumoto N, Imai J, Sakamoto H, Tanaka S, Ichikawa S, et al. Quantum tunneling injection of hot electrons in Au/TiO2 plasmonic photocatalysts. Nanoscale 2017. https://doi.org/10.1039/c7nr02310c.

[83] Snaith HJ, Grätzel M. The role of a "Schottky barrier" at an electron-collection electrode in solid-state dye-sensitized solar cells. Adv Mater 2006. https://doi.org/10.1002/adma.200502256.

[84] Gavin Conibeer, Nozik Arthur J, Matthew C, Beard Nozik AJ, Conibeer G, Beard MC. Advanced Concepts in Photovoltaics. Royal Society of Chemistry; 2014.

[85] Zhiqun Lin JW. Low-cost Nanomaterials: Toward Greener and More Efficient Energy Applications. Springer; 2014.

[86] Gu F, Huang W, Wang S, Cheng X, Hu Y, Lee PS. Open-circuit voltage improvement in tantalum-doped TiO2 nanocrystals. Phys Chem Chem Phys 2014. https://doi.org/10.1039/c4cp01655f.

[87] Lewis GN, Calvin M. The color of organic substances. Chem Rev 1939. https://doi.org/10.1021/cr60081a004.

[88] Maddah H, Jhally A, Berry V, Behura S. Highly efficient dye-sensitized solar cells with integrated 3D graphene-based materials. In: Graphene-based 3D Macrostructures Clean Energy Environ. Appl. Royal Society of Chemistry; 2021. p. 205–36.